Journal of Colloid and Interface Science 725 (2027) 141320

Contents lists available at ScienceDirect

Journal of Colloid And Interface Science

journal homepage: www.elsevier.com/locate/jcis

On the rapid growth and departure of nucleate bubbles in boiling on hydrophobic surfaces

Jinming Zhang [a,b], Sai Raja Gopal Vadlamudi [b,*], Uwe Hampel [b,c], Yunhua Gan [a,*], Angelica Cecilia [d], Tomáš Faragó [d], Marcus Zuber [d], Elias Hamann [d], Tilo Baumbach [d], Wei Ding [b,e,**]

[a] School of Electric Power Engineering, South China University of Technology, Guangzhou 510640, People's Republic of China
[b] Institute of Fluid Dynamics, Helmholtz-Zentrum Dresden-Rossendorf (HZDR), Dresden 01328, Germany
[c] Institute of Power Engineering, Technische Universität Dresden, Dresden 01062, Germany
[d] Institute for Photon Science and Synchrotron Radiation, Karlsruhe Institute of Technology, Hermann-von-Helmholtz-Platz 1, Eggenstein-Leopoldshafen 76344, Germany
[e] School of Environment Science and Spatial Informatics, China University of Mining and Technology, Xuzhou City, Jiangsu 221116, China

GRAPHICAL ABSTRACT

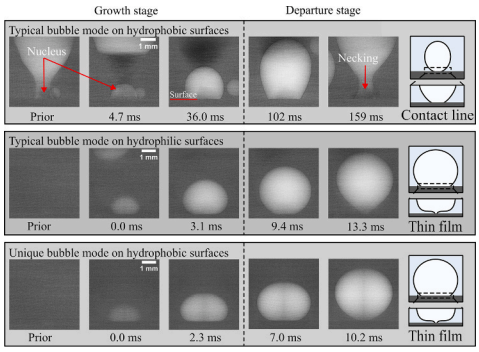

ARTICLE INFO

Keywords:
Nucleate boiling
Hydrophobic surface
Bubble dynamics
Near-surface thin liquid film

ABSTRACT

Hypothesis: Recent experiments have shown that tuning the initial wetting state of a hydrophobic surface before boiling gives rise to bubble behavior resembling that on hydrophilic surfaces. This contrasts with typical bubble behavior on hydrophobic surfaces, where bubble growth initiates from a residual vapor seed and results in slow growth and delayed departure. Here, we hypothesize that such wetting-state tuning modifies the near-surface liquid-vapor interfacial structure beneath the bubble, possibly through the formation of a near-surface thin liquid film, thereby altering bubble dynamics on hydrophobic surfaces.
Methods: Synchrotron X-ray imaging with high spatial resolution (2.44 μm) and a large field of view (~5 × 5 mm) was employed in pool boiling experiments to visualize the near-surface liquid-vapor interface and bubble evolution under different surface initial wetting states. Non-dimensional analysis of bubble growth and departure was performed to characterize bubble dynamics.

* Corresponding authors.
** Corresponding author at: Institute of Fluid Dynamics, Helmholtz-Zentrum Dresden-Rossendorf (HZDR), Dresden 01328, Germany.
E-mail addresses: s.vadlamudi@hzdr.de (S.R.G. Vadlamudi), ganyh@scut.edu.cn (Y. Gan), w.ding@hzdr.de (W. Ding).

https://doi.org/10.1016/j.jcis.2026.141320
Received 7 November 2025; Received in revised form 12 June 2026; Accepted 5 August 2026
Available online 10 August 2026

Findings: We identify a unique bubble mode on the PDMS-coated hydrophobic surface in which the near-surface liquid-vapor interfacial structure resembles that on hydrophilic surfaces, suggesting the possible presence of a near-surface thin liquid film. In addition, the associated non-dimensional parameters indicate rapid bubble growth similar to that observed during microlayer evaporation-assisted growth on hydrophilic surfaces. Notably, the bubble departs rapidly and smoothly, maintaining an oblate shape and a nearly constant apparent contact angle during departure without obvious hysteresis. A capillary relaxation timescale defined from bubble-shape deformation is comparable to the actual departure duration, suggesting that capillary forces contribute significantly to the rapid bubble departure.

1. Introduction

Boiling is an intensive phase change process characterized by the continuous formation and departure of vapor bubbles from a heated surface as the liquid transforms into vapor. Its critical role in various heat transfer applications (e.g., nuclear reactors, electronics cooling systems, and material processing) has spurred extensive research into underlying mechanisms. Notably, a key near-surface process in nucleate boiling is evaporation from the microlayer, which is typically less than 10 μm thick and trapped beneath a growing vapor bubble [1]. The microlayer gives rise to a nearly parallel liquid-vapor interfacial structure near the surface and prevent full vapor-solid contact at the bubble base. Such an interfacial structure maintains an extended thin-film evaporation area, where the maximum local heat flux can exceed 1 MW/m^2 [2], thereby serving as a critical mechanism for bubble growth [3]. The exact contribution of microlayer evaporation toward bubble growth depends on factors such as wetting characteristics, thermal boundary conditions, and microlayer morphology. To elucidate the microlayer heat transfer characteristics, numerous simulations and experiments have been conducted over the past decade, focusing on the microlayer formation mechanism [4–7] and its evaporation dynamics [8–10]. Despite this progress, these studies have mainly focused on hydrophilic surfaces, while studies on hydrophobic surfaces remain limited.

Hydrophobic surfaces are particularly relevant in boiling heat transfer as they significantly enhance the heat transfer coefficient due to the reduced incipience superheat for bubble nucleation and higher bubble nucleation density [11,12]. However, the bubble behaviors differ substantially from those on hydrophilic surfaces. Typically, bubble interface necking is consistently observed during bubble departure, leaving behind a visible bubble seed on the surface, with sizes ranging from hundreds of microns to millimeters [13–15]. Unlike individual bubble nucleation on hydrophilic surfaces with a waiting time between subsequent nucleation (hereafter referred to as the typical bubble mode on hydrophilic surfaces), the visible bubble seed directly initiates the subsequent bubble growth without any waiting time (hereafter referred to as the typical bubble mode on hydrophobic surfaces). In the typical hydrophobic mode, the near-surface liquid-vapor interface remains sharply connected to the heated surface through a localized contact line region, creating relatively large non-wetted areas that weaken surface heat removal [14]. Bubble growth in this mode is primarily driven by contact line evaporation, as evidenced by recent Lattice Boltzmann simulations [16] and experimental observations using infrared thermography [17]. Compared to microlayer evaporation, the average heat flux of contact line evaporation is considerably lower [18]. Nam et al. [19] observed that the bubble growth rate for the hydrophilic surface (silicon) is nearly 1–2 orders of magnitude higher, and the bubble life cycle is 60 times shorter than that for the hydrophobic surface (Teflon-coated silicon surface) under a similar low surface superheat. Moreover, such long-attached surface bubbles can readily coalesce under increased heat flux, expanding non-wetted areas and substantially degrading the critical heat flux [14,20,21].

The poor heat transfer performance of hydrophobic surfaces under high heat flux conditions has constrained their practical applications in boiling and thermal management. However, Allred et al. [22] demonstrated that thoroughly degassing a superhydrophobic textured surface (contact angle $\approx 160^\circ$) can alter the initial surface wetting condition, from one with visible residual gas/vapor seeds to one without visible residual seeds prior to bubble nucleation. This change was interpreted as a transition of the surface initial wetting state from a partially wetted Cassie–Baxter state to a fully wetted Wenzel state. In their approach, an additional immersion heater was employed to effectively remove residual gas on the surface, rather than relying on the heated surface for degassing, which could generate vapor bubbles that remain attached. Their results showed that changing the surface initial wetting condition can significantly improve both the heat transfer coefficient and the critical heat flux. Importantly, markedly different bubble dynamics were observed, characterized by individual nucleation and rapid bubble departure without residual bubble seeds on the surface. These observations suggest that appropriate wetting-state tuning may modify the near-surface liquid-vapor interfacial structure beneath bubbles on hydrophobic surfaces, possibly through the formation of a near-surface thin liquid film.

Recently, Moiz et al. [23] examined the bubble base dynamics using laser interferometry in a flow boiling experiment after removing the residual bubble seed on an indium tin oxide (ITO)-coated surface with a contact angle of $90 \pm 2^\circ$. A regular fringe pattern-an indicator of the microlayer presence-was observed beneath the bubble for only 0.3 ms. Subsequently, the fringe pattern disappeared, which was attributed to hydrodynamic contact line dewetting, as has been demonstrated in recent simulations [24–26]. This hydrodynamic dewetting is typically accompanied by the formation of an interface bulge near the contact line and promotes the depletion of the microlayer, particularly on low-wettability surfaces. As a result, the dryout area beneath the bubble is enlarged, leading to a delayed bubble departure due to contact line pinning. However, such bulge formation has not yet been confirmed experimentally. Furthermore, the ITO-coated surface cannot be regarded as purely hydrophobic, and it was stated that the wettability may transition toward hydrophilicity during boiling in a previous experiment [17]. Thus, whether tuning the initial wetting state of a hydrophobic surface can modify the near-surface liquid-vapor interfacial structure and thereby alter bubble dynamics remains an open question.

Progress on this question has been hindered by the difficulty of directly visualizing the near-surface microlayer and the associated bulge formation. To date, achieving such visualization remains challenging with common measurement techniques, including optical shadowgraphy and laser interferometry. In optical shadowgraphic imaging, light reflection and refraction limit resolution in the near-surface region beneath the bubble, whereas laser interferometry cannot resolve steep interface slopes [6]. Only Yu et al. [27] have demonstrated that synchrotron X-ray imaging may resolve such liquid-vapor interfaces owing to its high collimation and microscale spatial resolution. Building on this capability, we employ synchrotron X-ray imaging with high spatial resolution (2.44 μm) and a large field of view ($\sim 5 \times 5$ mm) in isolated bubble pool boiling experiments. This approach enables visualization of the near-surface liquid-vapor interface and the complete bubble evolution, allowing comparative analysis of their characteristics across different surface wettability. Complementary shadowgraphic imaging experiments were also performed to provide statistical insights into bubble dynamics.

2. Experimental methods

2.1. Boiling setup and measurement procedures

Two types of boiling surfaces were used in this study: a hydrophobic polydimethylsiloxane (PDMS)-coated glass surface and a hydrophilic silicon surface. The PDMS-coated glass surface was a commercially prepared 10 mm diameter, 0.17 mm thick coverslip with a flat PDMS layer (4DCell). The silicon surface was cut into a 10 mm diameter sample from a 0.5 mm thick polished silicon (100) wafer (Siegert Wafer GmbH). Before conducting the pool boiling experiments, surface wettability was characterized by measuring the static contact angle of a 9 μL water droplet ten times. As shown in Fig. 1a, the measured contact angles were 100.61 ± 0.48° and 64.35 ± 0.25° for the PDMS-coated glass surface and silicon surface, respectively. Pool boiling experiments were performed on both surfaces in a quartz glass boiling chamber (Fig. 1b) at atmospheric pressure with deionized water used as the working fluid. The deionized water was prepared using a water deionization system (Evoqua Water Technologies GmbH), with a measured conductivity of approximately 2 μS/cm. The boiling surface was heated using a bottom-mounted cartridge heater (24 V, 100 W, Friedr. Freek GmbH). An immersion heater (24 V, 100 W, Friedr. Freek GmbH) was placed in the chamber to heat the bulk liquid. K-type thermocouples (0.5 mm, TC Ltd) were embedded at the center of the rear side of the surface sample and in the chamber to measure the average temperature of the surface and bulk liquid.

We only considered isolated bubbles in the experiments to avoid the impact of neighboring bubbles. For the hydrophobic surface (PDMS-coated glass surface), the focus was on the first bubble formed after the onset of boiling, referred to as the "nucleate bubble", which did not originate from pre-existing large seeds. To generate such nucleate bubbles, a degassing procedure similar to that employed by Allred et al. [22] was conducted to remove residual gas from the hydrophobic surface. The bulk liquid was initially heated to its saturation temperature for at least one hour using both the immersion heater and cartridge heater to reduce the dissolved gas content in the bulk water. The system was then cooled to room temperature, allowing residual gas trapped on the surface to dissolve back into the bulk liquid, thereby reducing stable gas entrapment on the surface prior to the boiling experiment. This degassing procedure was repeated several times until no visible residual gas remained on the surface. Subsequently, the bulk liquid was reheated to saturation temperature, and a low power was supplied to the bottom cartridge heater to slowly increase the surface temperature and initiate bubble nucleation. As bubble nucleation could occur at arbitrary times and locations, measurements were performed continuously.

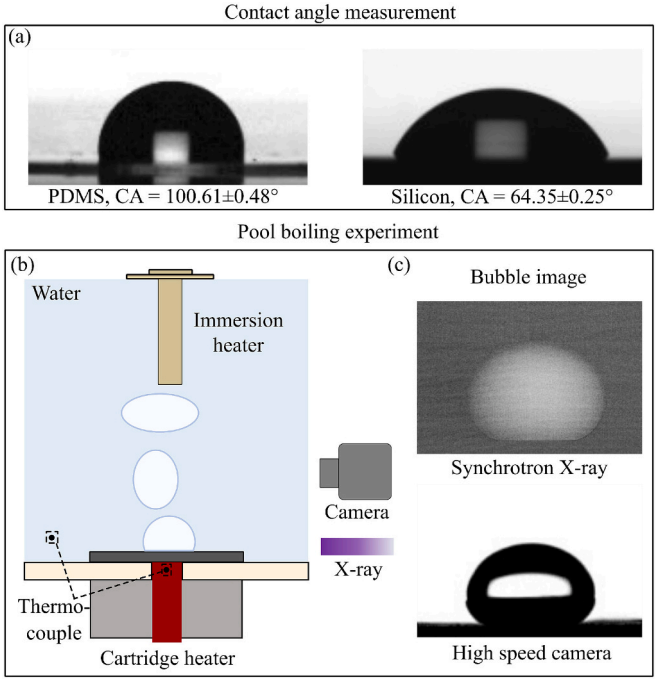

Fig. 1. Pool boiling experimental methodology. (a) Wetting characteristics of the PDMS-coated glass surface and the silicon surface, (b) schematic representation of the experimental setup, and (c) exemplary bubble images from synchrotron X-ray and a high-speed optical camera. The static contact angles are reported as mean ± standard deviation from 10 repeated measurements.

Following the capture of the nucleate bubble on the hydrophobic surface, a separate experiment was conducted. In this experiment, a conventional degassing procedure was performed without cooling the system to confirm that the observed nucleate bubble was not a result of surface hydrophobicity loss. This degassing procedure generated vapor seeds that remain attached to the surface. In this case, bubble growth occurred directly from these attached vapor seeds once the surface temperature reached 100 °C, and the bubble exhibited the typical behavior observed on hydrophobic surfaces. For the hydrophilic surface (silicon), a similar degassing procedure was employed, followed by heating the bulk liquid and surface until nucleation occurred, after which measurements were initiated once the surface temperature had stabilized. In this work, the surface initial wetting state was quantified operationally by the presence or absence of visible residual gas/vapor seeds before bubble nucleation. The partially wetted initial state was characterized by an attached residual vapor seed with a characteristic size of approximately 1 mm before the subsequent bubble cycle, whereas the fully wetted initial state corresponded to the absence of any visible residual gas/vapor seed within the imaging resolution.

The synchrotron X-ray radiography measurements were conducted with a white beam delivered from a superconducting wiggler located at the IMAGE beamline of the KIT Light Source [28]. After filtering with 1 mm pyrolytic graphite, the spectrum exhibited a photon flux density of 1.3×10^{14} pH s^{-1} mm^{-2} at the sample position (30 m from the source) with a broad energy distribution centered at 11 keV. The indirect detector consisted of a 24 μm thick LSO scintillator, optically coupled via a diffraction-limited microscope to a high-speed CMOS camera (PCO. dimax, Excelitas). The detector provided an effective pixel size of 2.44 μm, achieved through the combination of the 11 μm physical pixel size of the camera and the 4.5× magnification of the microscope. X-ray images were recorded at a speed of 1279 fps, with a field of view of 4.92 mm × 4.92 mm. In separate experiments, shadowgraphic imaging was performed using a high-speed optical camera (Q-VIT, AOS Technologies) with a macro lens (AT-X M100 PRO D, Tokina) to provide statistical insights into bubble dynamics. The optical system operated with a pixel size of approximately 12.5 μm and frame rates ranging from 2000 to 3500 fps. Exemplary bubble images from both measurements are shown in Fig. 1c. Note that bubbles captured from synchrotron X-ray imaging were preprocessed to remove the background (e.g., surface) for clarity.

2.2. Image processing and parameter extraction

All recorded bubbles were masked to extract bubble dynamics parameters using an in-house Python code, as illustrated in the workflow shown in Fig. 2. For the radiographic images, an image processing algorithm was developed to enhance the visualization of the bubble interface. First, an initial reference image was computed by averaging several early frames with minimal bubble presence. This reference image was subtracted from each frame to highlight the dynamic features of the bubble base regions. The resulting difference images were then smoothed using a Gaussian convolution filter to suppress high-frequency noise and enhance relevant features.

To identify bubble regions, a binary mask was generated by applying a threshold to the smoothed images. For each frame, the raw radiographic image was multiplied by the inverted mask and accumulated

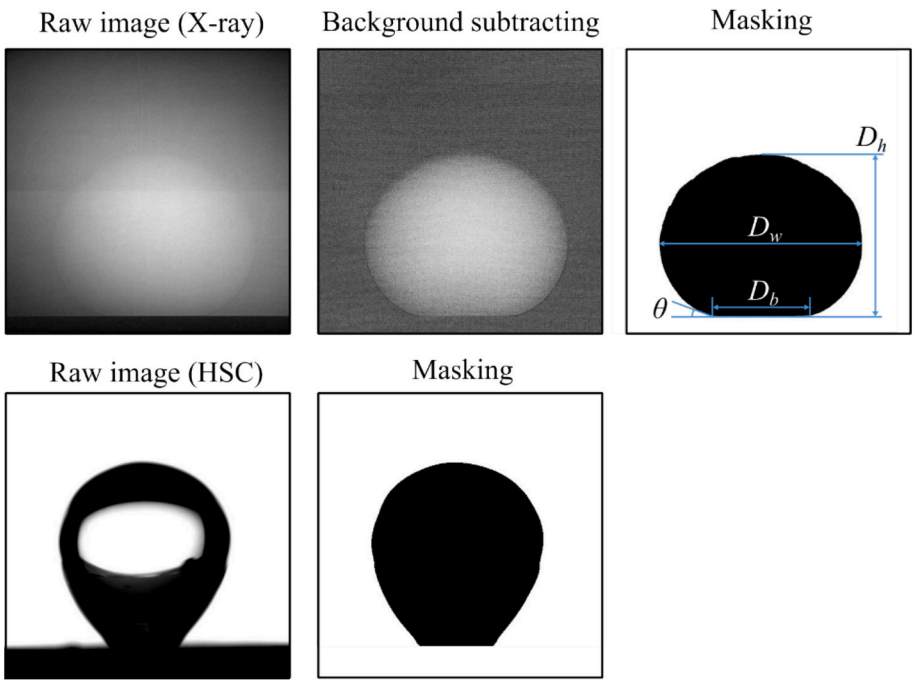

Fig. 2. Bubble image processing workflow for synchrotron X-ray imaging and shadowgraphic imaging.

into a matrix m. In addition, the inverted mask values were accumulated into a second matrix w, which recorded the count of non-bubble contributions at each pixel location. This selective accumulation ensured that only persistent non-bubble regions contributed to the final background estimation. Then, a refined reference image was computed by normalizing the accumulated intensity matrix m by the mask count matrix w, i.e., pixel-wise division. This refined reference represented the average background intensity of non-bubble areas, effectively removing transient features. Subtracting this refined reference image from the raw radiographs yielded processed images containing only the bubble interfaces while effectively removing the surface substrate. Finally, the processed synchrotron X-ray images were masked manually due to the inherent noise present in the radiographs. For the shadowgraphic images, the strong contrast between the bubble and the background allows automated segmentation using Otsu thresholding, which was applied to generate binary masks for bubble identification and masking.

Bubble dynamics parameters, including bubble equivalent diameter (D_{eq}), apparent bubble base diameter (D_b), bubble height (D_h), width (D_w), and the bubble apparent contact angle were extracted from the bubble mask. The bubble equivalent diameter (D_{eq}) was determined from the bubble volume (V) $D_{eq} = \sqrt[3]{\frac{6V}{\pi}}$. The bubble volume was calculated as the sum of the discretized volumes of disks, each with a thickness equivalent to one pixel, spanning from the base to the apex of the bubble:

$$V = \sum_{k=bubblebase}^{k=bubbleapex} \frac{\pi D_k^2 \times pixelsize}{4}, \quad (1)$$

in which D_k is the diameter of the disk. The bubble base diameter and apparent contact angle were extracted from the liquid-vapor interface immediately above the surface. The bubble height was defined as the maximum distance from the highest to the lowest point in the image mask, and the bubble width was the maximum distance from the far left to the far right.

2.3. Uncertainty analysis

The contact angle uncertainties were determined from ten repeated measurements and are reported as standard deviations. Thermocouples were calibrated in an oven from 60 °C to 160 °C in 10 °C increments, holding each step for 1 h to reach equilibrium. The maximum difference between the thermocouple and oven reference temperatures was less than 1 K, corresponding to a measurement uncertainty of ±1 K. The uncertainty of the extracted bubble dynamics parameters depends on the resolution of the image and the uncertainty of the edge. For each bubble image obtained from the synchrotron X-ray measurements, the masking procedure was performed five times manually to quantify the measurement reproducibility. This method is consistent with the previous work of Gerardi et al. [29]. The standard deviations obtained from these repeated masks were used as the error bars in the corresponding figures. For the shadowgraphic images, the uncertainty was determined by comparing manually processed bubble images with those obtained from automated masking at least three times for each selected image. The maximum uncertainty associated with the masking procedure was found to be ~5 pixels, corresponding to 75 μm and 67 μm for bubble equivalent diameter and bubble base diameter. The statistical bubble dynamics obtained from the synchrotron X-ray and shadowgraphic experiments were compared to ensure the reproducibility of the measured bubble behavior. The shadowgraphic imaging dataset used for this comparison included 21 bubble life cycles in total, consisting of 5 HPB-I, 3 HPB-II, and 13 HPL bubble life cycles, as detailed in **Supplementary Materials, Section A**.

3. Results and discussion

We first present representative bubble evolutions on both hydrophobic and hydrophilic surfaces. As shown in Fig. 3a–c, three distinct bubble modes are identified: two modes on the hydrophobic PDMS surface, depending on the initial surface wetting state, and one mode on the hydrophilic surface. Bubble mode I (HPB-I) is observed during continuous bubble generation on the PDMS surface in a partially wetted initial state under a surface superheat of 29 K, originating from the bubble seed left behind during the previous bubble departure. The bubble growth initiates directly from the bubble seed without a waiting period. In addition, a rather long life cycle, delayed departure, and a large bubble seed (~1 mm) left behind after departure are observed.

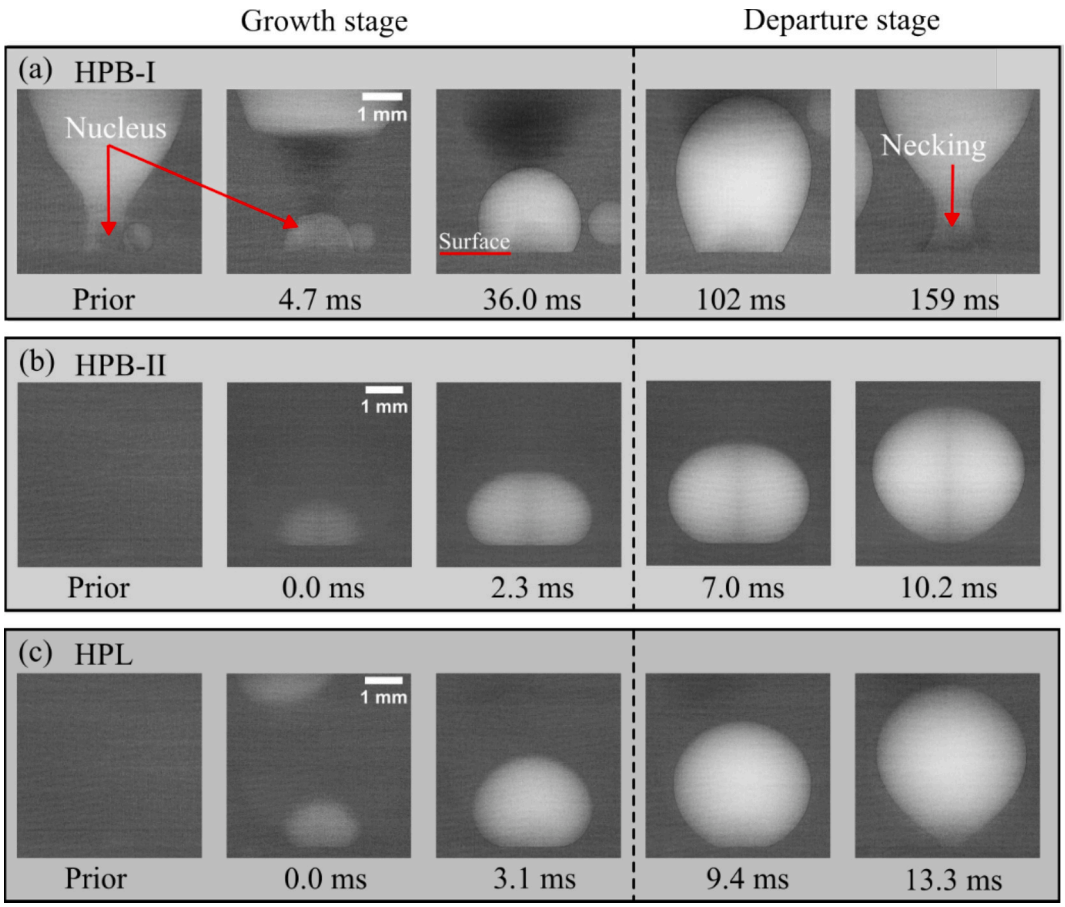

Fig. 3. Bubble modes observed on hydrophobic and hydrophilic surfaces. (a) Bubble mode HPB-I and (b) bubble mode HPB-II observed on the hydrophobic PDMS-coated glass surface under a surface superheat of 29 K, (c) bubble mode HPL observed on the hydrophilic silicon surface under a surface superheat of 25 K. The prior bubble is observed right before the inception of a new bubble life cycle (0 ms). The dashed line indicates the transition from the growth stage to the departure stage, marked by the bubble base diameter reaching its maximum. For clarity, the substrate surface was removed during image processing.

Subsequent nucleation consistently occurs from this residual seed in a repetitive manner. HPB-I represents the typical bubble mode on hydrophobic surfaces, such as on Teflon-coated silicon surface [13,19,30], PDMS-coated copper surface [22], and some ITO-coated sapphire (static droplet contact angle ~90°) [17,18]. Similar long bubble life cycle, delayed departure, and residual bubble seed have also been reported on oil-impregnated surfaces, where the bubble dynamics are associated with wetting-ridge-mediated interactions at the lubricant interface [31].

In contrast, bubble mode II (HPB-II), the first nucleate bubble that grows on the hydrophobic PDMS surface in a fully wetted initial state under the same superheat (29 K) without originating from any visible large seed, demonstrates markedly different characteristics. It exhibits individual bubble nucleation, rapid bubble growth and departure without any visible bubble seed left behind after bubble departure. In addition, the bubble life cycle is nearly 15 times shorter than that of HPB-I. Bubble mode on the hydrophilic surface (HPL), as shown in Fig. 3c, is observed during the continuous bubble generation on the silicon surface in a fully wetted initial state under a surface superheat of 25 K. Similar to HPB-II, HPL is also characterized by individual bubble nucleation, rapid bubble growth and departure, and a short bubble life cycle. HPL represents the typical bubble mode observed on hydrophilic surfaces, such as on borofloat glass surface [10,32], SiO_2-coated sapphire [18], fluoride tin oxide-coated borofloat glass [33], titanium [34], and some ITO-coated glass surfaces (static droplet contact angle ~45°) [2,35].

It should be noted that the difference between HPB-I and HPB-II is attributed to the different surface initial wetting states established before boiling. For HPB-II, no visible residual gas/vapor seed was observed on the surface before nucleation within the imaging resolution, corresponding to a fully wetted initial state in the operational sense used here. For HPB-I, an attached residual vapor seed remained on the surface before the subsequent bubble cycle, corresponding to a partially wetted initial state. This surface initial wetting state strongly affects the evolution of the near-surface liquid-vapor interface and thus the bubble dynamics. In addition, the higher observed incipience superheat for HPB-II can be attributed to the absence of residual vapor seeds, thereby requiring nucleation to occur. Moreover, bubble generation for HPB-II was found to be discontinuous, with exceptionally long waiting times of approximately tens of seconds. This waiting time is expected to decrease significantly with further increases in surface superheat. However, raising the superheat poses a risk of damaging the PDMS coating. Thus, bubble generation for HPB-II was investigated only at relatively low surface superheat to prevent surface degradation.

In the following sections, we begin in Section 3.1 with a detailed visualization of the near-surface liquid-vapor interface. Section 3.2 presents a quantitative analysis of bubble growth dynamics in relation to non-dimensional parameters from the literature that have been associated with microlayer evaporation-assisted rapid bubble growth. Finally, Section 3.3 examines the departure dynamics, highlighting how different bubble modes influence bubble base shrinkage, quantified through bubble shape deformation, apparent contact angle, and a proposed capillary relaxation timescale.

3.1. *Visualization of near-surface liquid-vapor interface*

The near-surface liquid-vapor interfacial dynamics are shown in

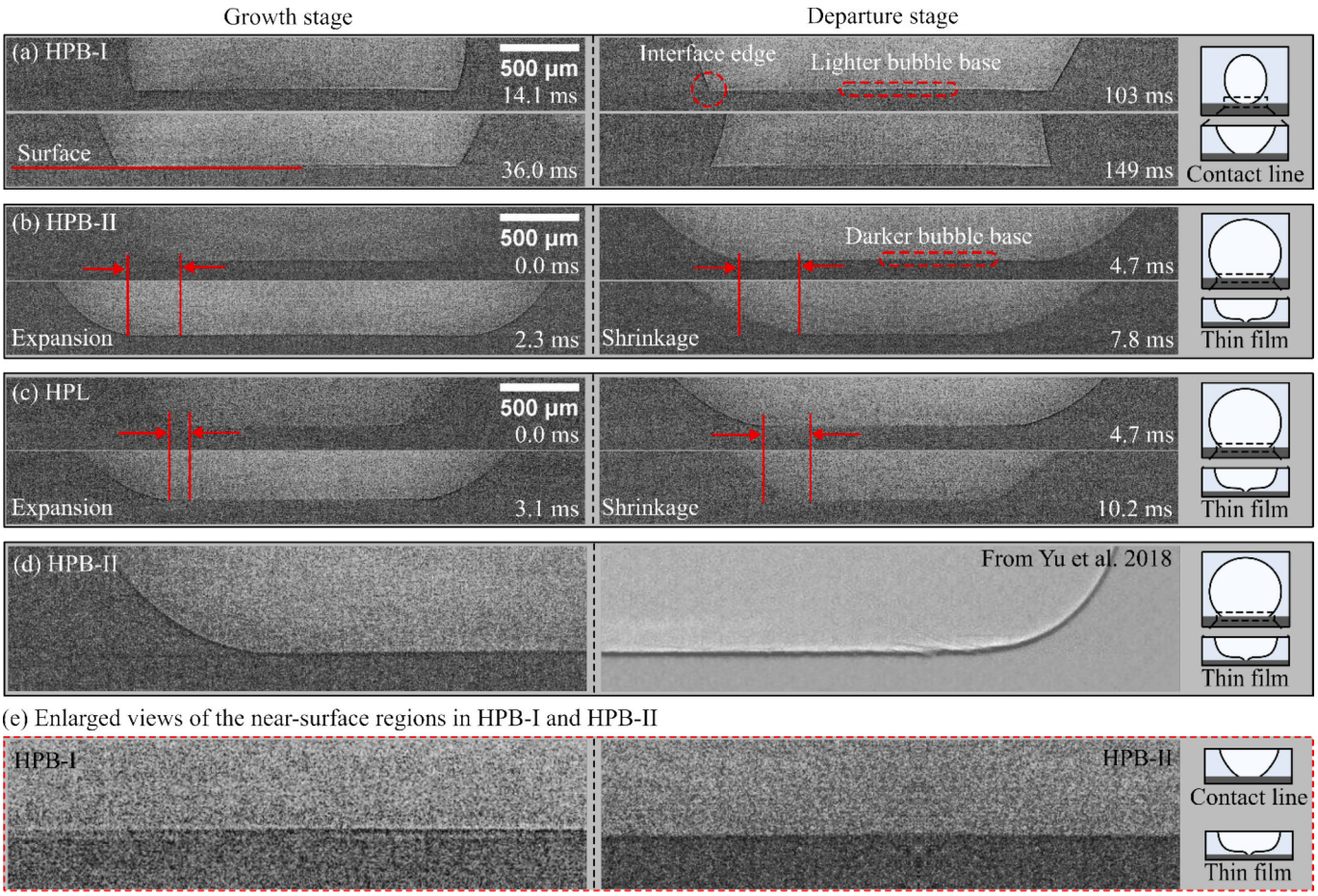

Fig. 4. (a–c) Synchrotron X-ray imaging results of liquid-vapor interfaces beneath the representative bubbles in Fig. 3, (d) comparison of the liquid-vapor interfaces between this study (HPB-II) and that reported by Yu et al. [27] for a silicon surface, (e) enlarged views of the near-surface regions in HPB-I and HPB-II. The schematic on the right illustrates the corresponding near-surface interfacial structures. The substrate surface was removed during image processing. Red vertical markers and arrows indicate the lateral extension of the apparent bubble base for visual comparison.

Fig. 4. For HPB-I, the interface remains convex with a large contact angle close to 90° for most of the bubble life cycle. Before departure, the interface transitions to a concave shape and breaks up through necking. A sharp interface edge is observed at the surface, connecting the bubble base to the bubble cap and marking the position of the contact line. In addition, the bubble base expands slowly during the growth stage and remains nearly constant in size throughout the majority of the departure stage, indicating strong contact line pinning. Generally, the microlayer formation is not expected underneath HPB-I-like bubbles, and bubble growth is predominantly driven by contact line evaporation [17] (see the schematic in Fig. 4).

Unlike HPB-I, the liquid-vapor interfaces in HPB-II and HPL exhibit a smooth edge at the outer boundary of the bubble base regions with relatively low contact angles. The bubble base undergoes rapid expansion and shrinkage. Fig. 4d compares the synchrotron X-ray image from our study (HPB-II) with that reported by Yu et al. [27] for a silicon surface (HPL), where microlayer formation has been observed. In both cases, the bubble base regions show a similar near-surface appearance, characterized by a nearly parallel feature along the surface. This similarity suggests comparable near-surface interfacial structure in HPB-II and HPL, despite their different surface wettability. More importantly, as shown in Fig. 4e, the bubble base region along the surface appears darker in HPB-II, but lighter in HPB-I. Detailed vertical X-ray intensity profiles across the PDMS-water, water-vapor, and PDMS-vapor interfaces are presented in **Supplementary Materials, Section B** to quantify the contrast differences observed between HPB-I and HPB-II. This contrast difference suggests that the near-surface interfacial structure in HPB-II differs from that in HPB-I. One possible interpretation is that HPB-II involves an additional near-surface thin film beneath the bubble, whereas HPB-I is more consistent with a contact line-dominated configuration.

Notably, the near-surface interface in Fig. 4 is less sharply resolved during the earliest stage of bubble growth, especially for HPB-II and HPL. This is because the present X-ray imaging was configured to capture the complete bubble dynamics, from nucleation to departure, within a single measurement window. Accordingly, a relatively large field of view of 4.92 mm × 4.92 mm was adopted, which limited the achievable temporal resolution. This limitation mainly affects the very initial stage of rapid bubble growth, during which the interface evolves too rapidly to be recorded with the same sharpness as in Ref. [27]. At later stages, the near-surface contrast remains sufficiently clear for a qualitative comparison among HPB-I, HPB-II, and HPL.

3.2. *Bubble growth dynamics*

The temporal evolutions of bubble growth dynamics parameters (bubble equivalent diameter D_{eq} and bubble base diameter D_b) for three bubble modes corresponding to the representative bubble life cycles shown in Fig. 3 and Fig. 4 are presented in Fig. 5a. The evolution of D_{eq} follows a similar pattern for three bubble modes, with the primary difference being only the growth rate. Note that D_{eq} for HPB-I is shown only up to 102.4 ms, beyond which the bubble moves out of the field of view. For the bubble base diameter, slight oscillation can be seen for bubble mode HPB-I during the growth stage, and subsequently remains almost

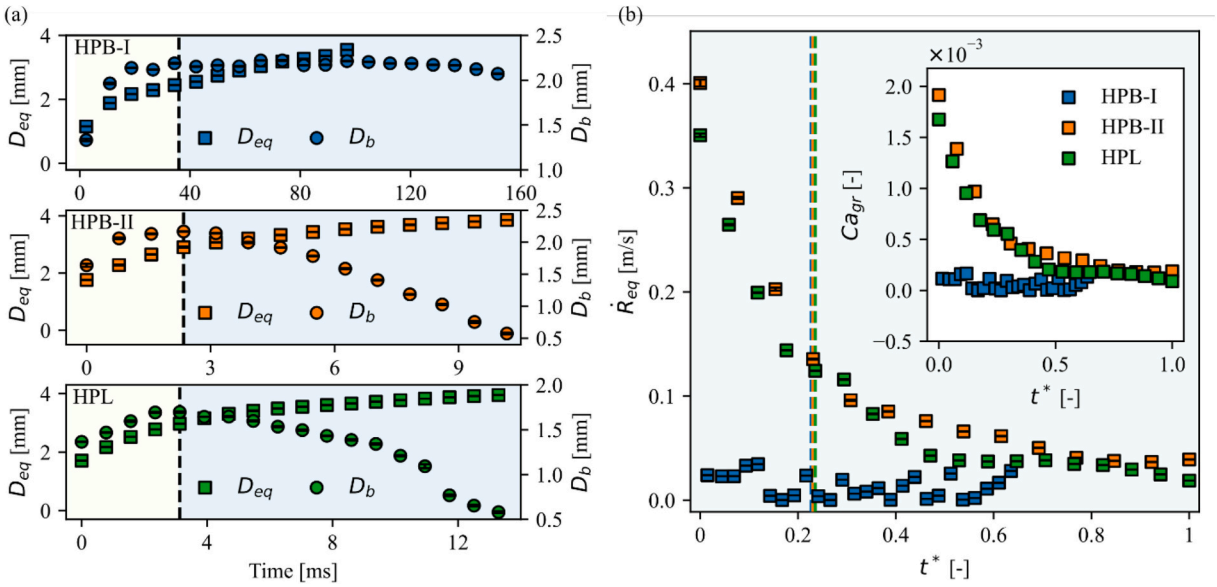

Fig. 5. (a) Evolution of bubble equivalent diameter D_{eq} and bubble base diameter D_b over time for the representative bubble life cycles, (b) evolution of bubble growth rate $\dot{R_{eq}} = dR_{eq}/dt$ and bubble growth-based Capillary number Ca_{gr} over non-dimensional time for the representative bubble life cycles. Dashed lines in (a) and (b) indicate the transition from the growth stage to the departure stage, marked by the bubble base diameter reaching its maximum. The error bars represent the standard deviations of the values obtained from five repeated manual masks, with maximum values of ±0.022 mm, ±0.013 mm, and ±0.0126 m/s for D_{eq}, D_b, and $\dot{R}_{eq}$, respectively.

constant in the departure stage. A similar evolution was reported by Jo et al. [15] on a Teflon-coated hydrophobic surface. In contrast, HPB-II and HPL show a rapid increase and subsequent decrease in D_b. In addition to the synchrotron X-ray imaging results, complementary shadowgraphic imaging results are provided in **Supplementary Materials, Section A**, along with statistical analysis of bubble behaviors from 21 bubble life cycles, including 5 HPB-I, 3 HPB-II, and 13 HPL bubble life cycles. Similar to the radiography measurements, two distinct bubble modes were identified from the shadowgraphic imaging results on the PDMS-coated hydrophobic surface, depending on the initial wetting states of the surface, i.e., the presence or absence of visible residual vapor/gas seeds prior to bubble nucleation. A good consistency is observed in the evolution of non-dimensional bubble equivalent diameter ($D^*_{eq} = D_{eq}/D_{eq,max}$) and base diameter ($D^*_b = D_b/D_{b,max}$) across multiple bubble life cycles within each bubble mode, indicating that the emergence of each bubble mode is reproducible, depending on the surface wettability and the presence of a visible bubble seed.

The bubble growth rate ($\dot{R_{eq}} = \frac{dR_{eq}}{dt}$, $R_{eq} = \frac{D_{eq}}{2}$) over the non-dimensional time ($t^* = t/t_{max}$) is depicted in Fig. 5b. For HPB-I, $\dot{R_{eq}}$ oscillates strongly while remaining at a low value of below 0.03 m/s. On the other hand, for both bubble modes HPB-II and HPL, $\dot{R_{eq}}$ starts at high values of approximately 0.4 m/s and continuously decreases throughout their life cycles. To provide further insight into bubble growth, the evolution of the bubble growth-based Capillary number Ca_{gr} for each bubble mode is examined:

$$Ca_{gr} = \frac{\mu \dot{R_{eq}}}{\sigma}, \tag{2}$$

where μ is the liquid dynamic viscosity and σ is the surface tension between the liquid and gas phase. The exact initial value of Ca_{gr} is of great importance, as it directly correlates with the microlayer formation. In recent direct numerical simulations, the hydrodynamic formation of microlayer under various initial Capillary numbers has been examined [24,26,36]. The results have emphasized the critical role of liquid viscous stress near the surface in microlayer formation. In particular, when the viscous stress is sufficiently high relative to capillary forces (e.g., $Ca \sim O(10^{-3})$ Giustini [26]), a thin liquid layer can be effectively trapped during bubble expansion. In the present experiments, Ca_{gr} in HPB-II and HPL initiates from a high value of $\sim 2 \times 10^{-3}$ and decreases continuously throughout the rest of the bubble life cycle. In addition, it is reasonable to anticipate an even higher initial Ca_{gr} value as the very initial stage of bubble growth is not captured due to temporal resolution limits (see bubble images in Fig. 3b and c). The initial Ca_{gr} values were also evaluated statistically based on the shadowgraphic imaging dataset, which included 21 bubble life cycles in total, consisting of 5 HPB-I, 3 HPB-II, and 13 HPL bubble life cycles (see **Supplementary Materials, Section A**) and are reported as $(3 \pm 2) \times 10^{-4}$ for HPB-I, $(3.2 \pm 0.9) \times 10^{-3}$ for HPB-II, and $(3.6 \pm 0.6) \times 10^{-3}$ for HPL.

To date, the critical value of the bubble growth-based capillary number Ca_{gr} required for the formation of microlayer remains uncertain, and it appears to be influenced by surface wettability. It is believed that highly wettable surfaces require lower Ca_{gr}, whereas less wettable surfaces demand higher values to sustain microlayer formation. In cases where Ca_{gr} is insufficient, contact line dewetting and the associated formation of an interface bulge may occur, potentially leading to the hydrodynamic collapse of the thin film and a transition to the contact line regime [7,25]. Nevertheless, no direct evidence of contact line dewetting or bulge formation was found in either our experiments or in those of Yu et al. [27] (see Fig. 4d).

Recent boiling experiments on hydrophilic surfaces have also reported that the initial rapid growth stage, driven by near-surface thin film evaporation, results in sufficient bubble growth inertia to overcome capillary forces [37]. To further evaluate this effect, we consider the bubble growth-based Weber number:

$$We_{gr} = \frac{\rho_l (\dot{R_{eq}})^2 D_{eq}}{\sigma}, \tag{3}$$

in which ρ_l is the liquid density. A value of $We_{gr} \gg 1$ has been associated with thin film evaporation-assisted rapid bubble growth on hydrophilic surfaces. The maximum observed We_{gr} exceeds 3 for bubble mode HPB-II (~5) and HPL (~3.5). Similar to Ca_{gr}, the initial We_{gr} is expected to be higher, on the order of $O(10)$. Such a large We_{gr} has only been observed in microlayer evaporation-driven growth on hydrophilic surfaces

[23,38,39]. By contrast, the bubble growth driven by contact line evaporation results in a maximum We_{gr} of only 0.18 for bubble mode HPB-I throughout the bubble life cycle. The maximum We_{gr} values were also evaluated statistically based on the same shadowgraphic imaging dataset (see **Supplementary Materials, Section A**) and are reported as 0.27 ± 0.04 for HPB-I, 7.7 ± 2.3 for HPB-II, and 4.1 ± 1.1 for HPL. The scatter in Ca_{gr} and We_{gr} within each bubble mode reflects variations in the initial bubble growth rate, which may arise from factors such as fluctuations in local liquid superheat prior to nucleation and nanoscale surface heterogeneities [49]. Nevertheless, it can be found that both the initial Ca_{gr} and the maximum We_{gr} for bubble mode HPB-II remain statistically one order of magnitude larger than those for HPB-I. This indicates that HPB-II undergoes rapid growth that is distinct from the slow growth of HPB-I. As mentioned above, the larger Ca_{gr} indicates that viscous stress associated with rapid bubble expansion becomes more significant relative to capillary forces, which favors liquid entrainment near the surface. Meanwhile, the larger We_{gr} indicates that bubble growth inertia is much stronger relative to capillary forces. These features indicate rapid bubble growth similar to that observed during microlayer evaporation-assisted growth in HPL, whereas HPB-I remains in a low Ca_{gr}, low We_{gr} regime, associated with slow bubble growth and contact line-dominated evaporation. Therefore, the similar near-surface liquid-vapor interfacial structure observed for HPB-II and HPL, along with the consistently higher Ca_{gr} and We_{gr} values, suggests that a near-surface thin liquid film may be present beneath the bubble in HPB-II. Nevertheless, the present X-ray measurements do not directly resolve the thickness or exact morphology of this liquid film.

The high We_{gr} sustains a hemispherical bubble shape during the growth stage. In the departure stage, when $We_{gr} < 1$, capillary forces become relatively more important, driving the transition toward a spherical shape and causing base shrinkage, as illustrated in Fig. 3. Besides capillary forces, buoyancy may also influence bubble dynamics as the bubble grows larger. To assess the relative impact of buoyancy compared to capillary forces, we consider the bubble Eötvös number:

$$Eo = \frac{\Delta\rho g D_{eq}^2}{\sigma}, \tag{4}$$

where $\Delta\rho$ is the density difference between the liquid and gas phase, and g is the gravitational acceleration. In addition, the bubble aspect ratio is defined to discuss bubble shape dynamics accurately: $\varepsilon = \frac{D_w}{D_h}$. The evolutions of Eo, We_{gr}, and ε over the non-dimensional time for the representative bubble life cycles are shown in Fig. 6. It can be seen that Eo evolves almost identically for bubble mode HPB-II and HPL. During the growth stage, $Eo < 1$ and $We_{gr} > 1$, indicating that bubble growth inertia is sufficient to overcome both buoyancy and capillary forces. At the end of the bubble growth stage for both bubble modes HPB-II and HPL We_{gr} reduces to ~1 ($t^* \approx 0.3$), likely due to the depletion of the thin film. The consistent value of this critical We_{gr} has been reported by Vadlamudi et al. [37] and Moiz et al. [39] on a hydrophilic glass surface. In the departure stage, Eo for all three bubble modes exceeds 1 while We_{gr} becomes less than 1. In this case, bubble buoyancy becomes more important, resulting in upward bubble movement.

The associated bubble shape factor $\varepsilon = \frac{D_w}{D_h}$ shows a similar pattern for HPB-II and HPL: it begins with an initial value around 2, corresponding to an approximately hemispherical shape. Subsequently, $\in$ decreases until the end of the bubble life cycle. On the other hand, the evolution of ε for HPB-I exhibits strong oscillations owing to the contact line pinning. As mentioned above, the bubble tends to retain its shape in the hemisphere in the growth stage due to the high We_{gr}. During this period, the

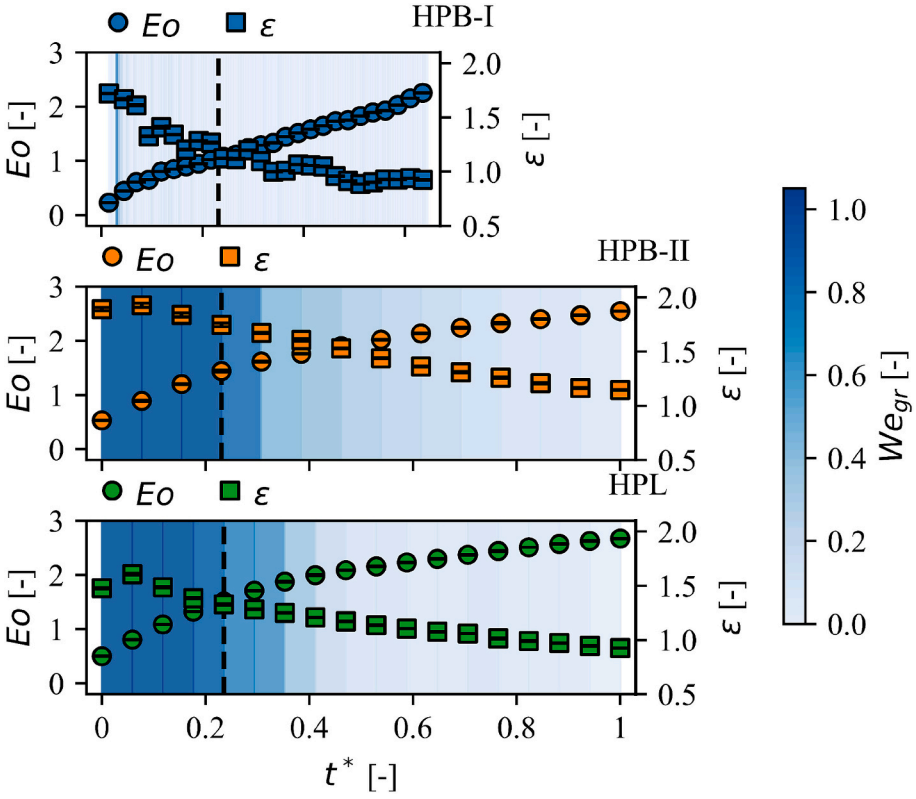

Fig. 6. Evolution of Eötvös number $Eo = \frac{\Delta\rho g D_{eq}^2}{\sigma}$ and aspect ratio $\varepsilon = \frac{D_w}{D_h}$ over non-dimensional time for the representative bubble life cycles, with the color gradient representing the bubble growth-based Weber number $We_{gr} = \frac{\rho_l (\dot{R}_{eq})^2 D_{eq}}{\sigma}$. Dashed lines indicate the transition from the growth stage to the departure stage, marked by the bubble base diameter reaching its maximum. The error bars represent the standard deviations obtained from repeated manual masking, with maximum values of 0.015 and 0.02 for Eo and ε, respectively.

rapid bubble growth process dictates the bubble dynamics, e.g., bubble shape change. Notably, ε for bubble mode HPB-II remains larger than 1 by the end of the bubble life cycle (1.15), indicating a flat bubble (as shown in the bubble images in Fig. 3). In contrast, ε for HPL reaches a lower value (0.93). Furthermore, the observed near-surface liquid-vapor interface in Fig. 4 exhibits a convex profile for HPL before departure, whereas for HPB-II the interface remains concave, highlighting a fundamental difference in interfacial structure during the departure stage.

Given the nearly identical evolution of *Eo* and the negligible bubble growth inertia during the departure stage, the differences in bubble and near-surface liquid-vapor interfacial shape evolution raise an intriguing question: what drives these disparities, and how do they influence the bubble departure dynamics? Bubble departure is critical to boiling heat transfer, as it directly determines the liquid rewetting of the heater surface [20]. This aspect will be explored further in Section 3.3 on bubble departure dynamics, with additional insights drawn from bubble shape deformation and bubble apparent contact angle evolutions.

3.3. Bubble departure dynamics

In an ideal bubble departure, where contact line pinning and other perturbative effects (e.g., liquid agitation) are absent, the bubble is expected to transition from an oblate to a spherical shape and then lift off directly from the surface. Since capillary forces are expected to contribute significantly to bubble shape relaxation during the departure stage, the oblate-sphere bubble shape transition may exhibit characteristics resembling a quarter of a Lamb mode ($N = 2$) oscillation. The characteristic duration for this transition can thus be estimated as one quarter of the capillary timescale $2\pi\sqrt{\frac{\rho_l R_{eq}^3}{8\sigma}}$ [40,41], which represents the period of a complete oscillation cycle. Here, R_{eq} is the equivalent bubble radius at the end of the growth stage.

For a quantitative assessment of the shape transition during the departure stage, we further define a normalized bubble shape deformation as $\varepsilon_\Delta = (D_w - D_{eq})/D_{eq}$, which characterizes the deviation of the bubble shape from a perfect sphere. The evolution of ε_Δ for the representative bubble life cycles is shown in Fig. 7. The time instants corresponding to the experimentally observed oblate-sphere transition and one quarter of the theoretical capillary timescale after the growth stage are marked as $t_{\text{transition}}$ and τ_{cap}, respectively. As observed, bubble departure in each mode deviates from the ideal process. However, the duration of the oblate-sphere shape transition for both HPB-I and HPL roughly matches τ_{cap}, indicating that the observed shape relaxation is broadly consistent with the capillary-relaxation timescale. For HPL, the subsequent evolution of ε_Δ remains nearly constant, and $t_{\text{transition}}$ coincides with the point at which the growth rate enters a low plateau ($t^* \approx 0.53$, see Fig. 5b). This correspondence suggests a shift in the bubble growth mechanism from thin film evaporation to contact line evaporation, likely caused by film depletion. A similar change in the dominant growth mechanism has also been noted by Kangude and Srivastava [18]. In contrast, the bubble in HPB-II remains oblate throughout its life cycle, and $t_{\text{transition}}$ is vastly underestimated. The prolonged oblate-to-sphere transition may be associated with additional near-surface effects, such as liquid inertia effects of the surrounding liquid and the possible near-surface thin film beneath the bubble [42,43]. Such observation is consistent with a persistent liquid film undergoing only limited depletion during departure, thereby facilitating smoother departure with

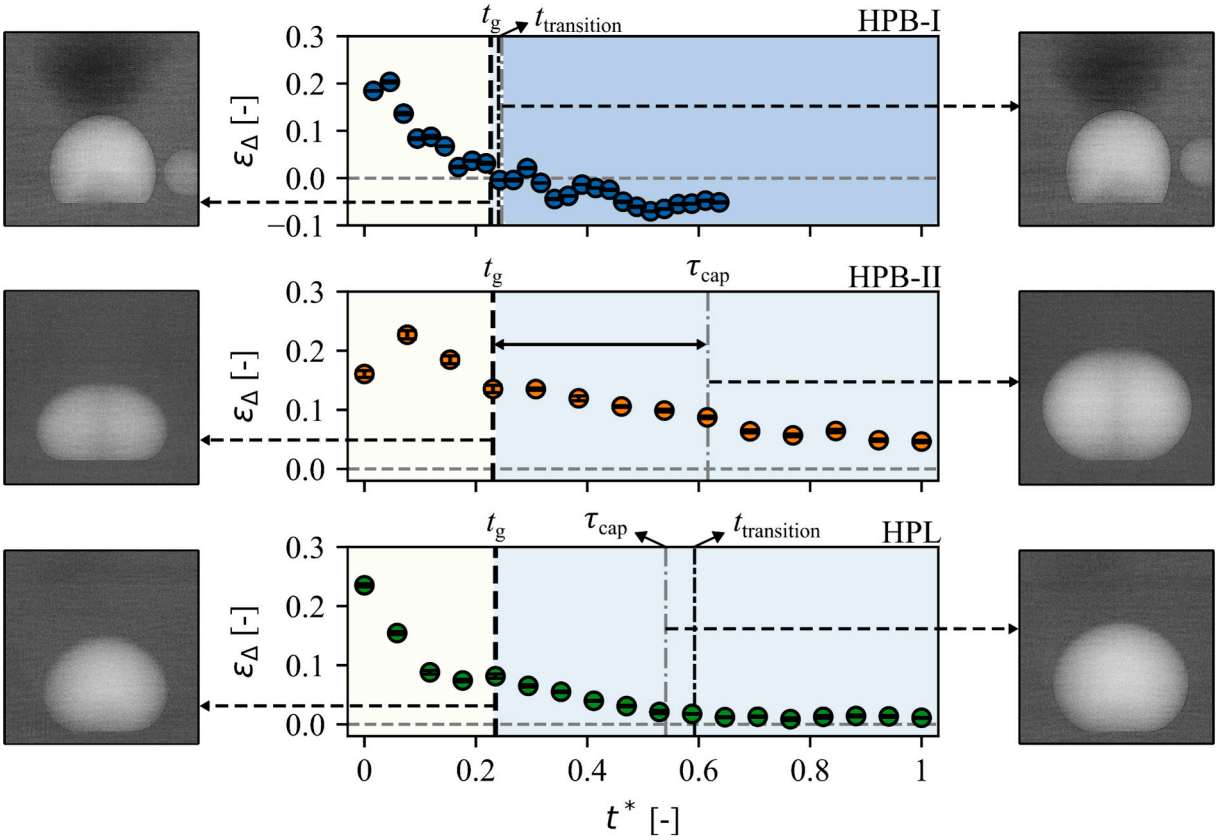

Fig. 7. Evolution of the normalized bubble shape deformation, $\varepsilon_\Delta = \frac{D_w - D_{eq}}{D_{eq}}$, for the representative bubble life cycles. A positive ε_Δ indicates an oblate bubble, zero denotes a spherical shape, and a negative value corresponds to a prolate bubble. The time instants corresponding to the end of the bubble growth stage, one-quarter of the capillary timescale, and the bubble oblate-sphere transition time after the growth stage are marked as t_g, τ_{cap}, and $t_{\text{transition}}$, respectively. The error bars represent the standard deviations obtained from repeated manual masking, with the maximum value of 0.07.

reduced contact-line pinning.

To gain insights into the thin film depletion, we further analyze the bubble base dynamics by tracking the evolution of the apparent bubble base and the corresponding apparent contact angle, as reported in previous studies of Bucci et al. [34,44]. Using an infrared camera, they tracked the motion of the contact line on a titanium surface and compared it with the expansion of the apparent bubble base. Their findings revealed that the contact angle begins to increase as the apparent bubble base approaches the actual bubble base, indicating significant thin film depletion. Therefore, the increase in the apparent contact angle can be considered a reliable indicator of significant thin film depletion.

A particular advantage of the synchrotron X-ray images compared to the shadowgraphic images is that they allow the apparent contact angle to be evaluated directly at the surface. Fig. 8 depicts the evolution of the apparent contact angle and the non-dimensional bubble apparent base diameter over non-dimensional time. The apparent contact angle for all bubble modes decreases rapidly during the growth stage. In the departure stage, the contact angle for HPB-I exhibits oscillations and gradually increases. By the end of the bubble life cycle, it exceeds 90°, accompanied by the formation of a neck in the bubble interface (see bubble images in Fig. 3). For HPL, the apparent contact angle begins to increase significantly at $t^* \approx 0.47$ after the growth stage. Notably, the three time instants of the increase in apparent contact angle ($t^* \approx 0.47$), the transition of the bubble shape to a sphere ($t^* \approx 0.59$), and the onset of the plateau in the growth rate ($t^* \approx 0.53$) roughly coincide, suggesting that contact line pinning significantly influences the bubble dynamics. The apparent contact angle for HPB-II remains stable in the departure stage, suggesting that the 'apparent base' and 'actual base' do not converge during the departure stage. This observation suggests minimal depletion of the near-surface thin film in HPB-II and is also consistent with the smooth oblate-sphere shape transition observed during the departure stage. It is important to note that the variation in contact angle dynamics is linked to contact line pinning on the surface, as the advancement of a contact line on a solid surface requires an increase in the apparent contact angle to overcome the viscous and surface resistance [45].

In addition, a bubble departure timescale is defined as $\tau_d = \frac{R_b}{\dot{R}_b}$ to characterize the bubble base shrinkage. Here, R_b is the bubble base radius and $\dot{R}_b$ is the bubble base velocity. The magnitude of the bubble base velocity is considered since we primarily focus on the departure stage. This timescale is represented as the color gradient in Fig. 8. As observed, τ_d is considerably larger in HPB-I than in other bubble modes during the departure stage and exhibits significant oscillations. For HPL, τ_d also shows slight oscillations, while in the case of HPB-II, it decreases smoothly throughout the departure process. Consequently, the duration of bubble base shrinkage in HPB-II (7.8 ms) is shorter than that in HPL (10.2 ms), despite a larger maximum base diameter in HPB-II (2.17 mm) compared to HPL (1.70 mm), as shown in Fig. 5a. In other words, the bubble base shrinkage in HPB-II proceeds at a higher rate. Consistent bubble departure dynamics were observed in the complementary dataset from the shadowgraphic imaging experiments in **Supplementary Materials, Section A**.

To highlight the complex bubble departure dynamics, we introduce a ratio to characterize the deviation of the bubble departure process from the capillary relaxation process. In Fig. 7, evolutions of the bubble shape deformation $\varepsilon_\Delta = (D_w - D_{eq})/D_{eq}$ in the departure stage show significant variation among the three observed bubble modes. Accordingly, we consider the maximum $(D_w - D_{eq})$ after the growth stage as a characteristic length. This length represents the largest deviation from sphericity and characterizes the deformation relaxed during departure. The corresponding capillary relaxation timescale $\tau_{c,d}$ is defined as:

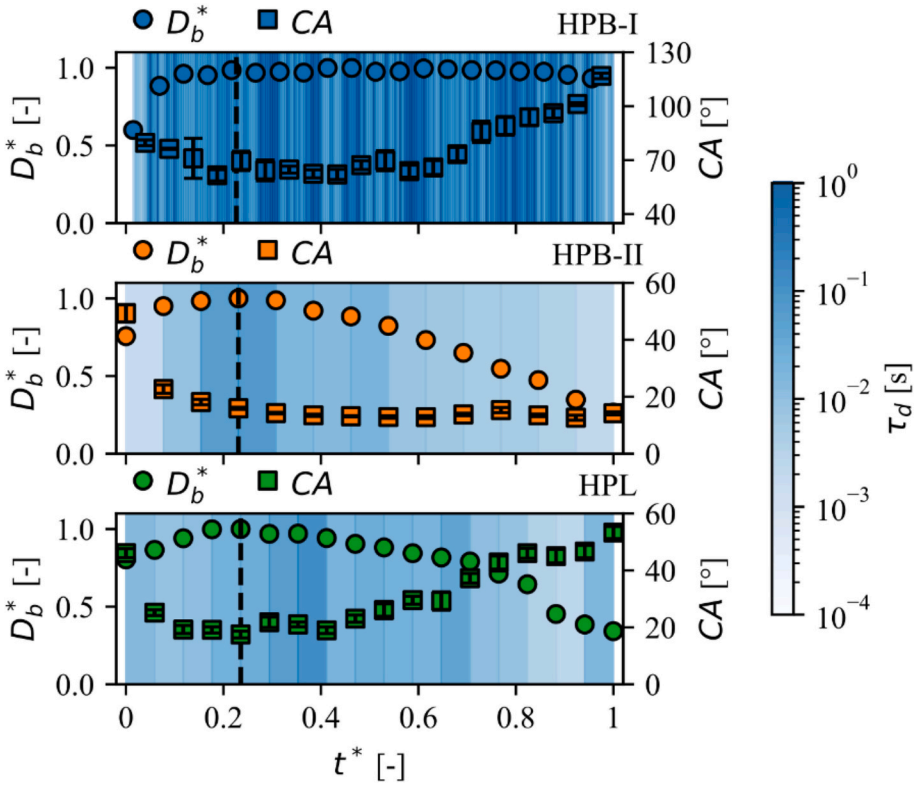

Fig. 8. Evolution of the non-dimensional bubble base diameter, and apparent contact angle over non-dimensional time for the representative bubble life cycles, with the color gradient representing bubble departure timescale $\tau_d = \frac{R_b}{\dot{R}_b}$. Dashed lines mark the transition between the growth and departure stages. The error bars represent the standard deviations obtained from five repeated manual masks, with a maximum value of ~±11°.

$$\tau_{c,d} = \sqrt{\frac{\rho_l (D_w - D_{eq})^3}{\sigma}}. \quad (5)$$

Any significant deviation from $\tau_{c,d}$ implies the influence of additional effects, e.g., bubble buoyancy, bubble growth, contact line pinning, and liquid inertia effect other than capillary forces (which is a function of deformation). Hence, to quantify this deviation, we define the time ratio as $\tau^*_{c,d} = \frac{\tau}{\tau_{c,d}}$, where τ is the actual bubble departure duration. We also reference the previously defined bubble shape factor ε and Eötvös number *Eo* to characterize the oblate bubble shape and bubble buoyancy immediately after the growth stage.

Fig. 9 presents a contour plot spanning 21 bubble life cycles from the shadowgraphic imaging dataset. This plot displays ε and *Eo*, with the color gradient representing $\tau^*_{c,d}$. Complementing the X-ray imaging results, multiple bubble life cycles obtained from the shadowgraphic imaging experiment with various bubble departure sizes are included for comparison (see **Supplementary Materials, Section A** for more details). Note that the surface superheat for the continuous bubble generation modes (i.e., HPB-II and HPL) within each experiment (radiography and shadowgraphy imaging) was maintained at the same value. As observed, *Eo* varies widely in each bubble mode in Fig. 9. Similar distributions of *Eo* have also been reported in previous experiments conducted under identical conditions [10,46–48], owing to the inherently stochastic nature of boiling. This arises from factors such as fluctuations in local liquid superheat prior to nucleation and nanoscale surface heterogeneities [49]. Nevertheless, ε has a good consistency within each bubble mode. In addition, for bubbles with similar *Eo* values (e.g., $Eo \sim 1.3$), τ and $\tau^*_{c,d}$ for HPL are consistently larger than those for HPB-II, indicating that the buoyancy is not a dominant factor determining bubble departure. For HPB-I, $\tau^*_{c,d}$ remains significantly larger than the other bubble modes, exceeding 1.5×10^3 regardless of ε. This indicates that bubble departure deviates drastically from the capillary relaxation process, primarily due to the influence of contact line pinning. Among all bubble modes, $\tau^*_{c,d}$ for HPB-II is the smallest, remaining below 25. This indicates that bubble departure in HPB-II is qualitatively more consistent with capillary relaxation than that in the other observed bubble modes. Nevertheless, the remaining mismatch suggests that additional near-surface effects may also be involved, as discussed above, including liquid agitation and liquid inertia effects. It is also worth noting that the surface superheat varies from 17 K to 29 K for the bubble cycles shown in Fig. 9, yet the bubble dynamics exhibits a strong consistency in both ε and $\tau^*_{c,d}$, suggesting that surface property plays a more significant role in governing these non-dimensional parameters.

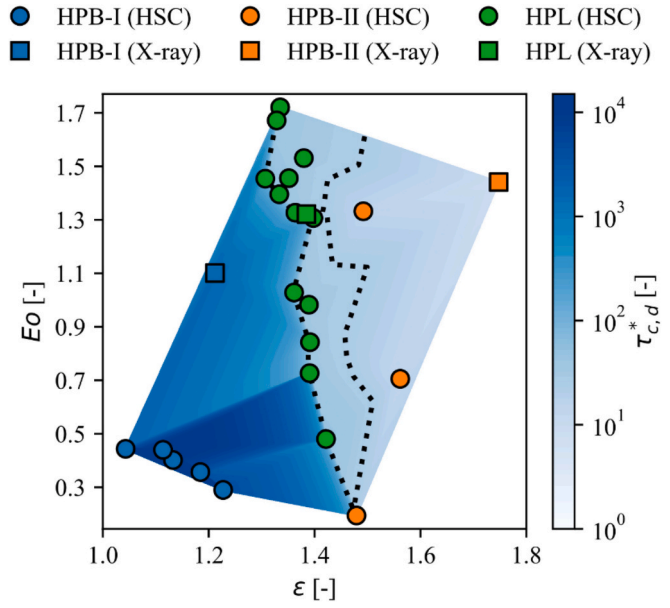

Fig. 9. Contour plot of the bubble shape factor $\varepsilon = \frac{D_w}{D_h}$ and *Eo* at the end of the growth stage for all bubble life cycles, with the color gradient representing the ratio of actual duration of bubble departure τ and capillary time scale $\tau_{c,d}$. Dashed lines mark the boundary of $\tau^*_{c,d}$.

4. Conclusions

Building on the previous experimental findings that an initially fully wetted superhydrophobic surface enables individual bubble nucleation and rapid departure, resembling those on hydrophilic surfaces [22], we hypothesize that wetting-state tuning may modify the near-surface liquid–vapor interfacial structure beneath bubbles on a hydrophobic surface, possibly through the formation of a near-surface thin liquid film. In this work, we utilized synchrotron X-ray imaging to investigate the bubble and near-surface liquid-vapor interfacial dynamics on a hydrophobic PDMS-coated surface. By tuning its initial wetting state to a fully wetted condition, we identified a bubble mode (HPB-II) in which the bubble and near-surface interface behave similarly to the typical bubble mode on hydrophilic surfaces (HPL), suggesting the possible presence of a thin liquid film underneath. The associated analysis of non-dimensional parameters, including the initial bubble growth-based Capillary number ($Ca_{gr} \sim O(10^{-3})$) and Weber number ($We_{gr} \sim O(10)$), indicates rapid bubble growth similar to that observed during microlayer evaporation-assisted growth on hydrophilic surfaces [26,37].

Furthermore, bubbles in HPB-II depart more smoothly and rapidly, maintaining an oblate shape with an almost constant apparent contact angle throughout the departure stage. These observations stand in sharp contrast with the HPL and HPB-I bubbles and with previously reported bubble dynamics on both hydrophilic and hydrophobic surfaces, where contact line pinning leads to an increasing apparent contact angle and delayed departure [15,18,34]. The comparison of the bubble apparent contact angle evolution in HPB-I and HPB-II suggests limited depletion of the near-surface liquid film throughout the bubble life cycle in HPB-II, which may contribute to the altered bubble departure dynamics. To characterize this bubble departure process, we introduced a capillary relaxation timescale based on bubble shape deformation and compared it with the actual departure duration. The smaller deviation between the capillary relaxation timescale and the actual departure duration in HPB-II, compared with other bubble modes, suggests that capillary forces contribute significantly to the rapid bubble departure and base shrinkage. These findings demonstrate a previously unreported bubble mode on the present PDMS-coated hydrophobic surface enabled by tuning the initial surface wetting state, revealing a possible interfacial regime in which a near-surface thin liquid film may be associated with rapid bubble growth and smooth departure.

While such behavior may be favorable for liquid rewetting, its implications for sustained boiling performance, including heat transfer coefficient and critical heat flux, were not quantified in the present study and therefore remain to be established. It should also be emphasized that the present X-ray measurements do not directly resolve the thickness or exact morphology of the near-surface thin film, and alternative thin-film or interfacial geometries cannot be fully excluded. Future improvements in synchrotron X-ray imaging or laser interferometry may help determine the morphology of this near-surface thin film on hydrophobic surfaces. In addition, a broader range of surface hydrophobicity would be required to clarify the role of surface wettability in controlling near-surface thin film morphology and bubble dynamics.

CRediT authorship contribution statement

Jinming Zhang: Writing – review & editing, Writing – original draft,

Visualization, Validation, Software, Methodology, Investigation, Formal analysis, Data curation, Conceptualization. **Sai Raja Gopal Vadlamudi:** Writing – review & editing, Validation, Methodology, Formal analysis. **Uwe Hampel:** Writing – review & editing, Supervision, Project administration, Funding acquisition. **Yunhua Gan:** Writing – review & editing, Supervision, Funding acquisition. **Angelica Cecilia:** Writing – review & editing, Validation, Methodology. **Tomáš Faragó:** Methodology. **Marcus Zuber:** Methodology. **Elias Hamann:** Methodology. **Tilo Baumbach:** Methodology. **Wei Ding:** Writing – review & editing, Validation, Supervision, Methodology, Funding acquisition, Conceptualization.

Declaration of competing interest

The authors declare that they have no known competing financial interests or personal relationships that could have appeared to influence the work reported in this paper.

Acknowledgments

This work was supported by the German Federal Ministry of Education and Research (BMBF) within the project H2Giga-SINEWAVE-OxySep, grant no. 03HY123E, and the Faculty of Mechanical Science and Engineering at TU Dresden. This work was also supported by the China Postdoctoral Science Foundation under Grant Number 2025M780563, the Guangdong Provincial Science and Technology Program Project under Grant Number 2025A0505020011, Guangdong Basic and Applied Basic Research Foundation under Grant Numbers 2025A1515140103 and 2025A1515110218, and the Education Department of Guangdong Province under Grant Number 2025KQNCX004..

Appendix A. Supplementary data

Supplementary data to this article can be found online at https://doi.org/10.1016/j.jcis.2026.141320.

Data availability

Data will be made available on request.

References

[1] J. Kim, Review of nucleate pool boiling bubble heat transfer mechanisms, Int. J. Multiph. Flow 35 (2009) 1067–1076, https://doi.org/10.1016/j.ijmultiphaseflow.2009.07.008.

[2] S. Jung, H. Kim, An experimental study on heat transfer mechanisms in the microlayer using integrated total reflection, laser interferometry and infrared thermometry technique, Heat Transf. Eng. 36 (2015) 1002–1012, https://doi.org/10.1080/01457632.2015.979109.

[3] T. Yabuki, O. Nakabeppu, Heat transfer mechanisms in isolated bubble boiling of water observed with MEMS sensor, Int. J. Heat Mass Transf. 76 (2014) 286–297, https://doi.org/10.1016/j.ijheatmasstransfer.2014.04.012.

[4] S. Jung, H. Kim, Hydrodynamic formation of a microlayer underneath a boiling bubble, Int. J. Heat Mass Transf. 120 (2018) 1229–1240, https://doi.org/10.1016/j.ijheatmasstransfer.2017.12.098.

[5] X. Zhang, I. El Mellas, N. Andreini, M. Magnini, The microlayer and force balance of bubbles growing on solid in nucleate boiling, Int. J. Multiph. Flow 183 (2025) 105049, https://doi.org/10.1016/j.ijmultiphaseflow.2024.105049.

[6] C. Tecchio, X. Zhang, B. Cariteau, G. Zalczer, P. Roca i Cabarrocas, P. Bulkin, J. Charliac, S. Vassant, V.S. Nikolayev, Microlayer in nucleate boiling seen as Landau–Levich film with dewetting and evaporation, J. Fluid Mech. 989 (2024) 1–20, https://doi.org/10.1017/jfm.2024.488.

[7] L. Bureš, Y. Sato, On the modelling of the transition between contact-line and microlayer evaporation regimes in nucleate boiling, J. Fluid Mech. 916 (2021) 1–23, https://doi.org/10.1017/jfm.2021.204.

[8] Y. Utaka, Y. Kashiwabara, M. Ozaki, Z. Chen, Heat transfer characteristics based on microlayer structure in nucleate pool boiling for water and ethanol, Int. J. Heat Mass Transf. 68 (2014) 479–488, https://doi.org/10.1016/j.ijheatmasstransfer.2013.09.063.

[9] Y. Utaka, K. Hu, Z. Chen, T. Morokuma, Measurement of contribution of microlayer evaporation applying the microlayer volume change during nucleate pool boiling for water and ethanol, Int. J. Heat Mass Transf. 125 (2018) 243–247, https://doi.org/10.1016/j.ijheatmasstransfer.2018.04.044.

[10] S. Narayan L, A. Srivastava, On the identification and mapping of three distinct stages of single vapor bubble growth with the corresponding microlayer dynamics, Int. J. Multiph. Flow 142 (2021) 103722, https://doi.org/10.1016/j.ijmultiphaseflow.2021.103722.

[11] B. Bourdon, P. Di Marco, R. Rioboo, M. Marengo, J. De Coninck, Enhancing the onset of pool boiling by wettability modification on nanometrically smooth surfaces, Int. Commun. Heat Mass Transf. 45 (2013) 11–15, https://doi.org/10.1016/j.icheatmasstransfer.2013.04.009.

[12] E. Forrest, E. Williamson, J. Buongiorno, L.W. Hu, M. Rubner, R. Cohen, Augmentation of nucleate boiling heat transfer and critical heat flux using nanoparticle thin-film coatings, Int. J. Heat Mass Transf. 53 (2010) 58–67, https://doi.org/10.1016/j.ijheatmasstransfer.2009.10.008.

[13] H. Jo, H.S. Ahn, S. Kang, M.H. Kim, A study of nucleate boiling heat transfer on hydrophilic, hydrophobic and heterogeneous wetting surfaces, Int. J. Heat Mass Transf. 54 (2011) 5643–5652, https://doi.org/10.1016/j.ijheatmasstransfer.2011.06.001.

[14] H.J. Jo, S.H. Kim, H.S. Park, M.H. Kim, Critical heat flux and nucleate boiling on several heterogeneous wetting surfaces: controlled hydrophobic patterns on a hydrophilic substrate, Int. J. Multiph. Flow 62 (2014) 101–109, https://doi.org/10.1016/j.ijmultiphaseflow.2014.02.006.

[15] H. Jo, H.S. Park, M.H. Kim, Single bubble dynamics on hydrophobic-hydrophilic mixed surfaces, Int. J. Heat Mass Transf. 93 (2016) 554–565, https://doi.org/10.1016/j.ijheatmasstransfer.2015.09.031.

[16] S. Gong, P. Cheng, Lattice Boltzmann simulations for surface wettability effects in saturated pool boiling heat transfer, Int. J. Heat Mass Transf. 85 (2015) 635–646, https://doi.org/10.1016/j.ijheatmasstransfer.2015.02.008.

[17] P. Kangude, A. Srivastava, Understanding the growth mechanism of single vapor bubble on a hydrophobic surface: experiments under nucleate pool boiling regime, Int. J. Heat Mass Transf. 154 (2020) 119775, https://doi.org/10.1016/j.ijheatmasstransfer.2020.119775.

[18] P. Kangude, A. Srivastava, Experiments to understand bubble base evaporation mechanisms and heat transfer on nano-coated surfaces of varying wettability under nucleate pool boiling regime, Int. J. Multiph. Flow 152 (2022) 104098, https://doi.org/10.1016/j.ijmultiphaseflow.2022.104098.

[19] Y. Nam, J. Wu, G. Warrier, Y. Sungtaek Ju, Experimental and numerical study of single bubble dynamics on a hydrophobic surface, J. Heat Transfer 131 (2009) 1–7, https://doi.org/10.1115/1.3216038.

[20] H. Kim, D.E. Kim, Effects of surface wettability on pool boiling process: dynamic and thermal behaviors of dry spots and relevant critical heat flux triggering mechanism, Int. J. Heat Mass Transf. 180 (2021) 121762, https://doi.org/10.1016/j.ijheatmasstransfer.2021.121762.

[21] E. Teodori, T. Valente, I. Malavasi, A. Moita, M. Marengo, A. Moreira, Effect of extreme wetting scenarios on pool boiling conditions, Appl. Therm. Eng. 115 (2017) 1424–1437, https://doi.org/10.1016/j.applthermaleng.2016.11.079.

[22] T.P. Allred, J.A. Weibel, S.V. Garimella, Enabling highly effective boiling from superhydrophobic surfaces, Phys. Rev. Lett. 120 (2018) 174501, https://doi.org/10.1103/PhysRevLett.120.174501.

[23] M. Moiz, S.R.G. Vadlamudi, A. Srivastava, Experiments to understand bubble base growth mechanism(s) on hydrophobic surfaces under the influence of bulk flow inertia during nucleate boiling regime, Int. Commun. Heat Mass Transf. 141 (2023) 106546, https://doi.org/10.1016/j.icheatmasstransfer.2022.106546.

[24] M. Saini, X. Chen, S. Zaleski, D. Fuster, Direct numerical simulations of microlayer formation during heterogeneous bubble nucleation, J. Fluid Mech. 984 (2024) 1–18, https://doi.org/10.1017/jfm.2024.236.

[25] A. Urbano, S. Tanguy, G. Huber, C. Colin, Direct numerical simulation of nucleate boiling in micro-layer regime, Int. J. Heat Mass Transf. 123 (2018) 1128–1137, https://doi.org/10.1016/j.ijheatmasstransfer.2018.02.104.

[26] G. Giustini, Hydrodynamic analysis of liquid microlayer formation in nucleate boiling of water, Int. J. Multiph. Flow 172 (2024) 104718, https://doi.org/10.1016/j.ijmultiphaseflow.2023.104718.

[27] D.I. Yu, H.J. Kwak, H. Noh, H.S. Park, K. Fezzaa, M.H. Kim, Synchrotron x-ray imaging visualization study of capillary-induced flow and critical heat flux on surfaces with engineered micropillars, Sci. Adv. 4 (2018) 37–42, https://doi.org/10.1126/sciadv.1701571.

[28] A. Cecilia, R. Simon, E. Hamann, M. Zuber, T. Faragó, D. Haenschke, M. Hurst, T. van de Kamp, S. Bauer, R. Spiecker, M. Czyzycki, S. Gasilov, A. Ershov, J.-T. Reszat, T. Baumbach, The IMAGE beamline at the KIT light source, J. Synchrotron Radiat. 32 (2025) 1036–1051, https://doi.org/10.1107/S1600577525003777.

[29] C. Gerardi, J. Buongiorno, L. Hu, T. McKrell, Study of bubble growth in water pool boiling through synchronized, infrared thermometry and high-speed video, Int. J. Heat Mass Transf. 53 (2010) 4185–4192, https://doi.org/10.1016/j.ijheatmasstransfer.2010.05.041.

[30] Y. Li, K. Zhang, M.C. Lu, C. Duan, Single bubble dynamics on superheated superhydrophobic surfaces, Int. J. Heat Mass Transf. 99 (2016) 521–531, https://doi.org/10.1016/j.ijheatmasstransfer.2016.03.098.

[31] Y. Zhou, C. Vandieren, S. Adera, Pool boiling of water on micro-nanostructured oil-impregnated surfaces, Int. J. Heat Mass Transf. 252 (2025) 127342, https://doi.org/10.1016/j.ijheatmasstransfer.2025.127342.

[32] L. Surya Narayan, A. Srivastava, Non-contact experiments to quantify the microlayer evaporation heat transfer coefficient during isolated nucleate boiling regime, Int. Commun. Heat Mass Transf. 122 (2021) 105191, https://doi.org/10.1016/j.icheatmasstransfer.2021.105191.

[33] M. Moiz, S.R.G. Vadlamudi, A. Srivastava, Experiments to understand microlayer and dry patch dynamics under subcooled nucleate flow boiling in a vertically

oriented rectangular channel, Phys. Fluids 35 (2023), https://doi.org/10.1063/5.0142177.
[34] M. Bucci, J. Buongiorno, M. Bucci, The not-so-subtle flaws of the force balance approach to predict the departure of bubbles in boiling heat transfer, Phys. Fluids 33 (2021), https://doi.org/10.1063/5.0036956.
[35] S. Jung, H. Kim, An experimental method to simultaneously measure the dynamics and heat transfer associated with a single bubble during nucleate boiling on a horizontal surface, Int. J. Heat Mass Transf. 73 (2014) 365–375, https://doi.org/10.1016/j.ijheatmasstransfer.2014.02.014.
[36] A. Guion, S. Afkhami, S. Zaleski, J. Buongiorno, Simulations of microlayer formation in nucleate boiling, Int. J. Heat Mass Transf. 127 (2018) 1271–1284, https://doi.org/10.1016/j.ijheatmasstransfer.2018.06.041.
[37] S.R.G. Vadlamudi, G.K. Sinha, A. Srivastava, S. Singh, Dynamic interaction of growing bubble and microlayer: need for reconciliation of experiments and theory in flow boiling, Appl. Phys. Lett. 121 (2022), https://doi.org/10.1063/5.0101747.
[38] S.R.G. Vadlamudi, M. Moiz, A. Srivastava, U. Hampel, W. Ding, On the quantification of microlayer contribution toward bubble growth under subcooled flow boiling regime, Phys. Fluids 36 (2024), https://doi.org/10.1063/5.0223460.
[39] M. Moiz, S.R.G. Vadlamudi, A. Srivastava, Comprehensive experimental thermal analysis of single bubble nucleation in vertical flow boiling: whole field temperature and microlayer dynamics, Int. J. Heat Mass Transf. 233 (2024) 126006, https://doi.org/10.1016/j.ijheatmasstransfer.2024.126006.
[40] M.S. Plesset, A. Prosperetti, Bubble dynamics and cavitation, Annu. Rev. Fluid Mech. 9 (1977) 145–185, https://doi.org/10.1146/annurev.fl.09.010177.001045.
[41] H. Lamb, Hydrodynamics, University Press, 1924.
[42] C.W.M. Van Der Geld, J.G.M. Kuerten, Axisymmetric dynamics of a bubble near a plane wall, J. Fluid Mech. 640 (2009) 265–303, https://doi.org/10.1017/S0022112009991340.
[43] C. Béguin, É. Pelletier, S. Étienne, Void fraction influence on added mass in a bubbly flow, Eur. J. Mech. B/Fluids 56 (2016) 28–45, https://doi.org/10.1016/j.euromechflu.2015.11.008.
[44] M. Bucci, A Theoretical and Experimental Study of Vapor Bubble Dynamics in Separate Effect Pool Boiling Conditions, Master's Thesis, University of Pisa, Italy, 2020 conducted at MIT,.
[45] D. Bonn, J. Eggers, J. Indekeu, J. Meunier, E. Rolley, Wetting and spreading, Rev. Mod. Phys. 81 (2009) 739–805, https://doi.org/10.1103/RevModPhys.81.739.
[46] A. Kossolapov, M.T. Hughes, B. Phillips, M. Bucci, Bubble departure and sliding in high-pressure flow boiling of water, J. Fluid Mech. 987 (2024) A35, https://doi.org/10.1017/jfm.2024.405.
[47] Y. Utaka, Y. Kashiwabara, M. Ozaki, Microlayer structure in nucleate boiling of water and ethanol at atmospheric pressure, Int. J. Heat Mass Transf. 57 (2013) 222–230, https://doi.org/10.1016/j.ijheatmasstransfer.2012.10.031.
[48] Z. Chen, Y. Utaka, On heat transfer and evaporation characteristics in the growth process of a bubble with microlayer structure during nucleate boiling, Int. J. Heat Mass Transf. 81 (2015) 750–759, https://doi.org/10.1016/j.ijheatmasstransfer.2014.10.058.
[49] M. Gallo, F. Magaletti, A. Georgoulas, M. Marengo, J. De Coninck, C.M. Casciola, A nanoscale view of the origin of boiling and its dynamics, Nat. Commun. 14 (2023) 6428, https://doi.org/10.1038/s41467-023-41959-3.